Chapter 1

Dielectric Barrier Discharge Microplasma Actuator for Flow Control

Kazuo Shimizu and Marius Blajan

Additional information is available at the end of the chapter

http://dx.doi.org/10.5772/intechopen.75802

Abstract

Dielectric barrier discharge (DBD) plasma actuators are a technology which could replace conventional actuators due to their simple construction, lack of moving parts, and fast response. This type of actuator modifies the airflow due to electrohydrodynamic (EHD) force. The EHD phenomenon occurs due to the momentum transfer from charged species accelerated by an electric field to neutral molecules by collision. This chapter presents a study carried out to investigate experimentally and by numerical simulations a micro-scale plasma actuator. A microplasma requires a low discharge voltage to generate about 1 kV at atmospheric pressure. A multi-electrode microplasma actuator was used which allowed the electrodes to be energized at different potentials or waveforms, thus changing the direction of the flow. The modification of the flow at various time intervals was tracked by a high-speed camera. The numerical simulation was carried out using the Suzen-Huang model and the Navier-Stokes equations.

Keywords: dielectric barrier discharge, microplasma, electrohydrodynamic flow, flow control, plasma actuator

1. Introduction

Active flow control is necessary in various industrial processes to improve system efficiency or to reduce environmental load [1]. In order to achieve flow control, mechanical actuators were developed and used. A new device for flow control was developed by Roth et al. in the 1990s [2]. A dielectric barrier discharge (DBD) was used and it was called a *plasma actuator*. The nonthermal plasma actuator operates at atmospheric pressure and compared with conventional types of actuators for flow control, has several advantages besides its simple construction, such as no moving parts and fast response [3, 4]. Plasma actuators for flow control were

investigated in applications for separation flow control [5–8] and noise reduction [8, 9]. The plasma actuator has an operating principle based on the electrohydrodynamic (EHD) phenomenon occurring due to the momentum transfer from ions accelerated by an electric field to neutral molecules by collision. Dielectric barrier discharge (DBD) and corona discharge are among the most common types of plasma actuators. A single DBD plasma actuator can induce a flow up to 7 m/s, and with a multiple DBD plasma actuator design, the value of induced flow can reach 11 m/s [10]. Various applications of flow control require different types of plasma actuators. For high-speed flow control, an induced flow speed of more than 7 m/s is necessary; thus instead of using a single DBD plasma actuator, the corona discharge could be used [11–15]. In the case of turbulent boundary-layer control for skin-friction drag reduction, millimeter-size discharge gap DBD plasma actuators were energized at peak-to-peak voltages of about 7 kV [16–19]. Research studies regarding the applications of plasma actuators involve turbulent boundary-layer separation control, steady airfoil leading-edge separation control, oscillating airfoils dynamic stall control, and circular cylinder wake control. According to various researchers, high values of the induced flow are desired. High values of the flow are obtained conventionally by energizing the plasma actuators at tens of kilovolts which are difficult to insulate and for which a large sized power supply is necessary. An effective actuation effect requires also a higher EHD force density that can be achieved using a micrometer order discharge gap plasma actuator, which lowers the discharge voltage and consequently requires lower power. Micro-sized plasma actuators were used for separation flow control and drag reduction [20–22]. A microplasma actuator was developed for flow control [23]. Similar electrode configurations were described in [24–28] but the required discharge voltages are more than 2 kV. Microplasma is a type of dielectric barrier discharge nonthermal plasma and its driven voltage is around only 1 kV. This technology could be used as a replacement of conventional technologies for surface treatment of polymers, indoor air treatment, biomedical applications, or flow control [29–32].

Measurements of microplasma actuators are difficult due to their micrometer size discharge gaps; thus, we have developed a numerical simulation of the induced flow based on the Suzen-Huang [33, 34] and Orlov [35] models. Due to the light emission from microplasma, observation and measurement of flow is difficult. Numerical simulations of the plasma actuator are carried out using the plasma fluid model and particle in cell model [36–39]. A simplified phenomenological model which does not model the species transport equations but can replicate the effects of the actuator in the air is the Suzen-Huang model [40]. Results close to the experimental data were obtained by various researchers who developed numerical simulations based on this model. It is less computationally expensive than solving the species transport equations [40, 41].

The microplasma actuator developed in our laboratory is thin and flexible and can be attached to any surface. To energize the actuator, small-sized power supplies are necessary; thus, a potential use for this actuator could be on drones. The electronic switching adds a greater flexibility in order to obtain flows in various directions. In comparison with macro-plasma actuators where the power supplies are bulky, the small-sized power supply necessary for a microplasma actuator adds little weight to the drone; also, less electrical insulation is necessary.

http://dx.doi.org/10.5772/intechopen.75802

2. Microplasma actuator

A microplasma actuator was developed for flow control. Due to its small size, the experimental results were difficult to obtain near the active electrodes; thus, a numerical simulation was developed in order to simulate the flow and add additional information about the flow. The experimental and numerical simulation results showed the capability of the microplasma actuator to control the flow.

2.1. Experimental study of microplasma actuator

2.1.1. Characteristics of microplasma actuator

A schematic of the typical construction of a plasma actuator and the induced air flow is shown in **Figure 1**. A pulse or alternating high voltage is applied to the two electrodes with a dielectric layer in between; thus, a plasma is generated at the surface of the electrodes [42]. An electrohydrodynamic (EHD) phenomenon occurs because ions are accelerated by the electric field and furthermore collide with neutral molecules; thus, a momentum transfer occurs and air flow is generated [21, 43].

A microplasma actuator that can be driven by a lower voltage of less than 2 kVpp was developed and investigated. Owing to their low discharge voltage, the applied high voltage could be controlled easily using semiconductor switches. The structure of the microplasma actuator is shown in **Figure 2** [44]. A dielectric layer consisted of a polymer film of 25-μm thickness sandwiched in between a high voltage electrode and a grounded electrode. Voltages less than 2 kVpp are enough to generate a microplasma due to the thickness of the 25-μm discharge gap. A pulse high voltage power supply was used to energize the actuator with the schematic shown in **Figure 3**. Four field-effect transistors (FETs) are used with a DC high voltage power supply. The microplasma actuator is energized by a positive pulse voltage while FETs 1 and 4 are in the ON state and by negative pulse voltage while FETs 2 and 3 are in the ON state, respectively.

Figure 4 shows the experimental setup used to visualize and investigate the air flow induced by the microplasma actuator. The microplasma actuator was set on a Z stage. A high voltage probe (Tektronix, P6105A) connected to an oscilloscope (Tektronix, TDS 3014) was used to

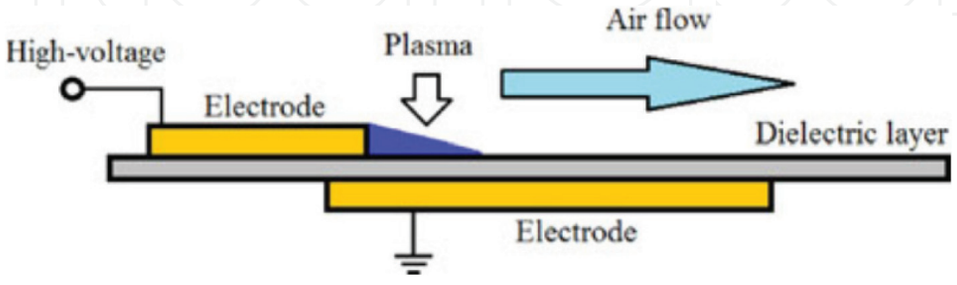

Figure 1. Typical construction of a plasma actuator. High voltage is applied to the electrodes with a thin dielectric layer in between.

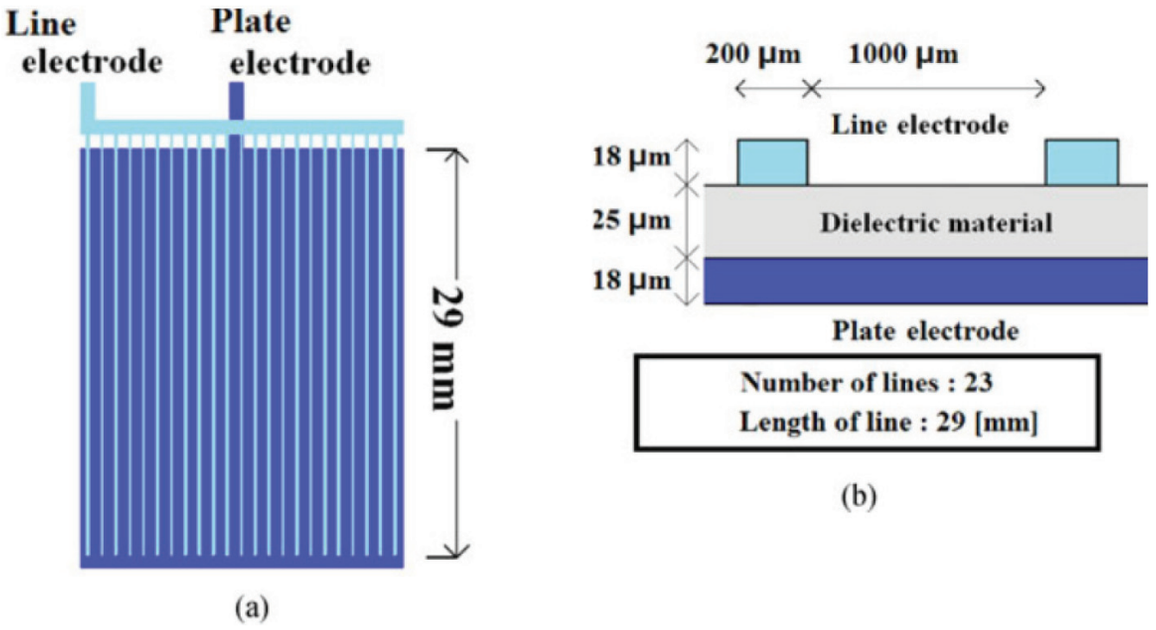

Figure 2. Geometry of the microplasma actuator. The four high voltage energized electrodes can be driven independently. (a) Top-view. (b) Cross-sectional view.

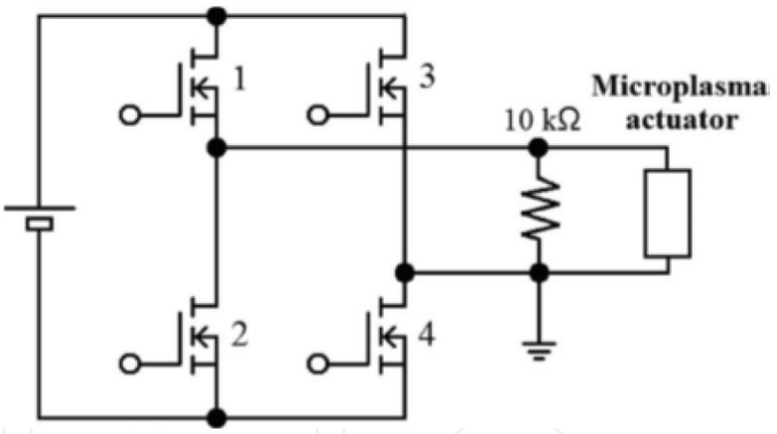

Figure 3. Schematic of pulsed high voltage source with semiconductor switches.

measure the discharge voltage. For the discharge current measurement, a current probe (Tektronix, P6021) connected to the oscilloscope was used. By multiplying the values of the voltage and current waveform measured with an oscilloscope, the discharge power was obtained for the pulse voltage. Furthermore, in order to calculate the discharge energy, the obtained discharge power waveform was integrated. Particle tracking velocimetry (PTV) was used as the method to measure the induced air flow by the microplasma actuator [45]. The microplasma actuator was placed inside an acrylic box and incense smoke with particles 0.3 μm in diameter [46] was inserted inside the box. For the measurement of the incense smoke particles, a laser particle counter (Kanomax, Model 3886) was used. For the flow measurements, a laser was used (Nd:YVO_4 532-nm) to irradiate the particles. The flow of tracer particles was recorded by a high-speed camera (Red Lake, Motionscope M3) having

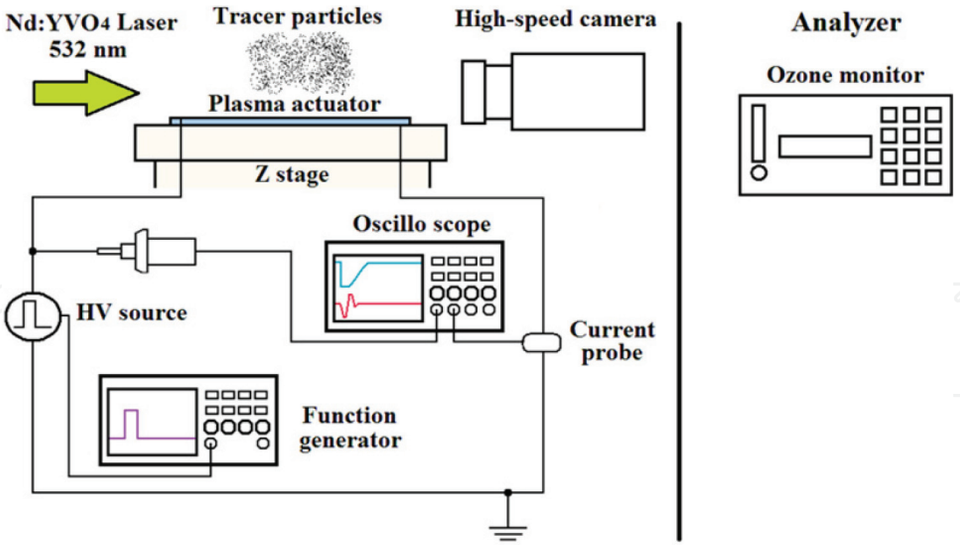

Figure 4. Experimental setup for visualization and measurement of the air flow induced by the microplasma actuator.

1280 × 1024-pixel resolution and 4000 Hz recording frequency. The area captured by the camera was 34 × 11 mm^2. The results were analyzed by the PTV method having a resolution of 1 mm in the *x*-axis and 0.5 mm in the *y*-axis. For the PTV method, steady state images of two continuous frames were used.

The Stokes number was calculated in order to estimate the ability of the incense smoke to follow the flow field [47], and the value was in the order of 10^{-5}; this is an acceptable flow tracing accuracy with error less than 1% [46]. Ozone concentration due to the microplasma was measured by an ozone monitor (Seki Electronics, SOZ-3300). The measurements were carried out by placing the microplasma actuator inside a glass tube which was connected to the ozone monitor at a distance of 90 cm.

The microplasma actuator could be energized by bipolar pulse as shown in **Figure 5** with *T* period and also positive and negative pulses as shown in **Figure 6(a)** and **(b)**. For both positive and negative pulses at a frequency of 2 kHz, the pulse width was 4 μs. The calculated energy consumption by integrating the discharge power waveform shown in **Figure 6** for a single pulse is shown in **Figure 7**. In order to have microplasma discharge, a voltage higher than 0.5 kV was necessary. The values of energy were almost the same for positive and negative pulses respectively; thus, at 1.4 kV, the calculated value of energy was about 800 μJ for both positive and negative pulses. This corresponds to an average power of 1.6 W.

Energy consumption was measured for a discharge voltage of 1.4 kV at various pulse frequencies for both polarities as shown in **Figure 8**. At 1 Hz, the energy consumption was about 650 μJ. With the increase of frequency, the single pulse energy consumption increased. This could be explained by the charges in plasma that due to the electric field were moved and trapped at the surface of the dielectric. These surface charges [48, 49], when the next opposite polarity is applied, will increase the electric field strength; furthermore, higher energy consumption for a single pulse was obtained with the increase of frequency. Due to recombination or diffusion, the surface charge will decrease in time.

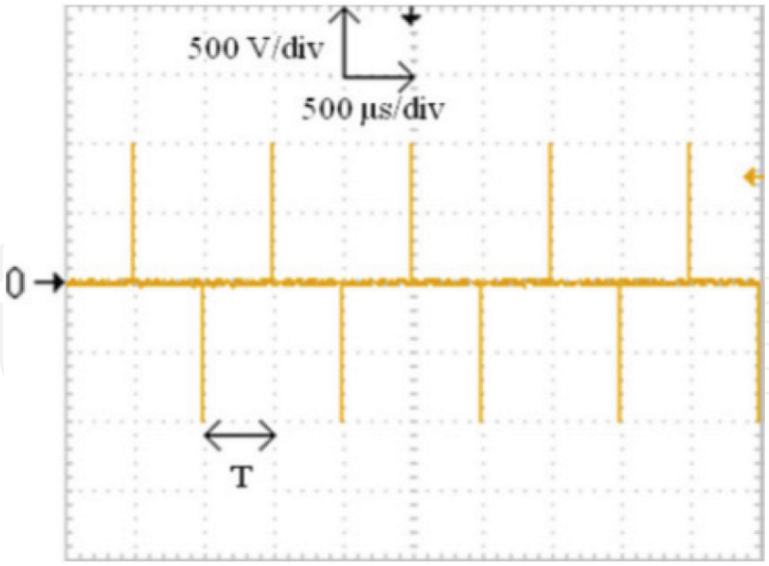

Figure 5. Waveform of pulsed high voltage applied to the microplasma actuator.

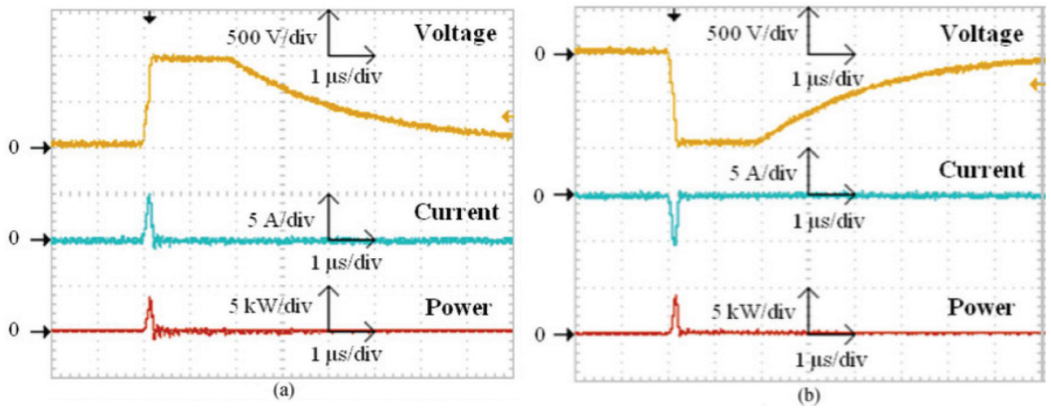

Figure 6. Waveforms of discharge voltage and corresponding discharge current and power. (a) Positive pulse. (b) Negative pulse.

Ozone (O_3) is harmful to humans due to its high oxidation ability, which is next to fluorine. The World Health Organization Air Quality Guidelines for Europe in its second edition imposed a value of 0.05 ppm as an 8-hours daily average concentration for ozone. The microplasma actuator generates ozone and the concentration of generated ozone was measured by energizing the actuator while it was rolled and inserted into an 8 mm diameter glass tube. An 1.5 L/min airflow was set inside the tube while the actuator was energized. The microplasma actuator was energized by a bipolar pulse with a frequency of 2 kHz. In **Figure 9** the characteristics of ozone concentration versus power consumption is shown. The microplasma actuator has an ozone yield of about 28 g/kWh, which is lower than what other researchers reported [50, 51]. Besides the fact that ozone causes damages to tissues, a higher concentration of ozone can cause the degradation of electrodes [52]. Thus, a low ozone yield is necessary for flow control applications [53].

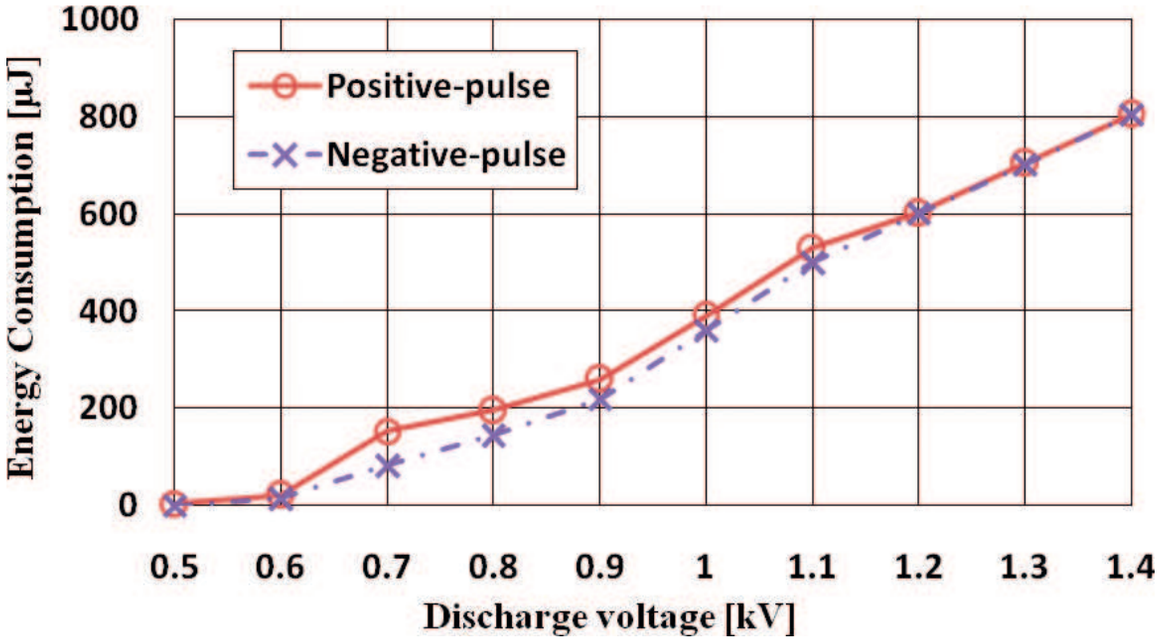

Figure 7. Energy consumption of single pulse versus discharge voltage for a pulse frequency of 2000 Hz.

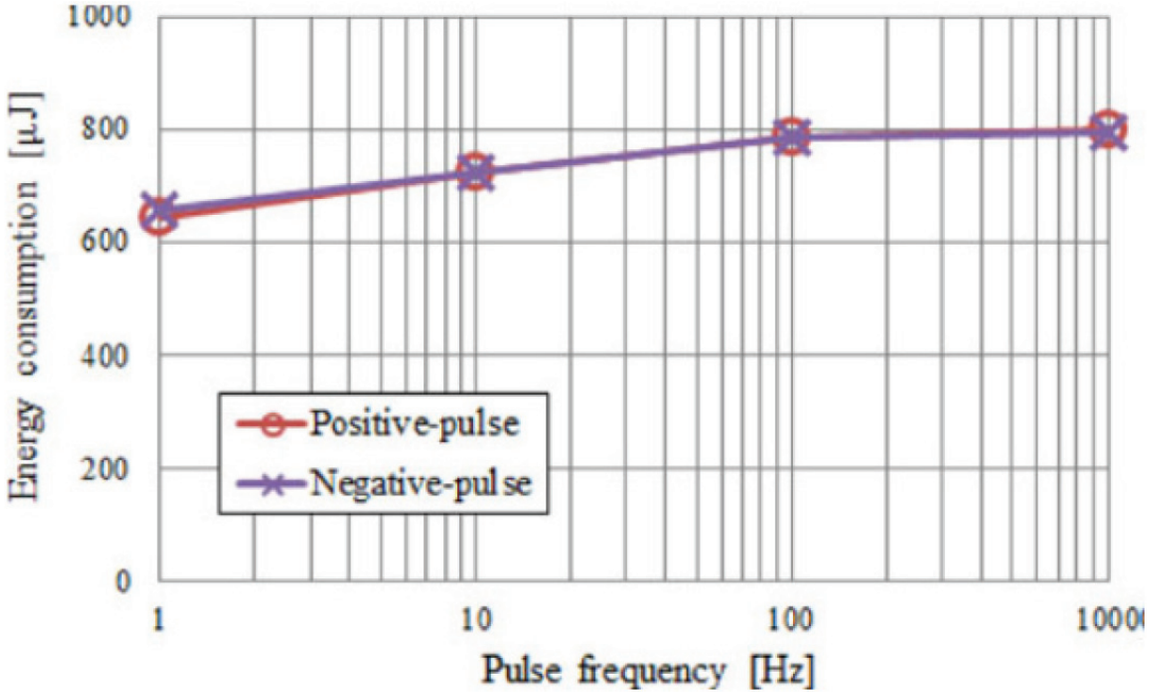

Figure 8. Energy consumption of a single pulse versus pulse frequency for a discharge voltage of 1.4 kV.

2.1.2. Flow control with microplasma actuator

The micro-scale plasma actuator, besides the requirement of low discharge voltage, has the advantage of easy integration due to its small size. A microplasma actuator similar to the one

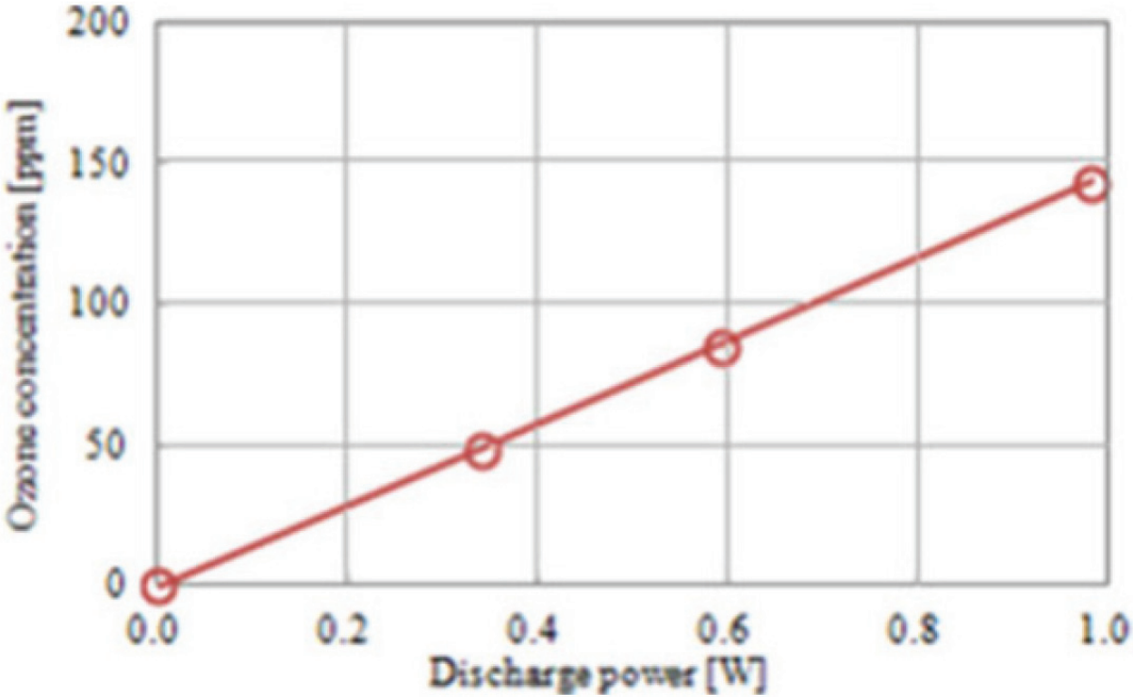

Figure 9. Ozone concentration measured while driving the microplasma actuator at 1.5 L/min. air flow.

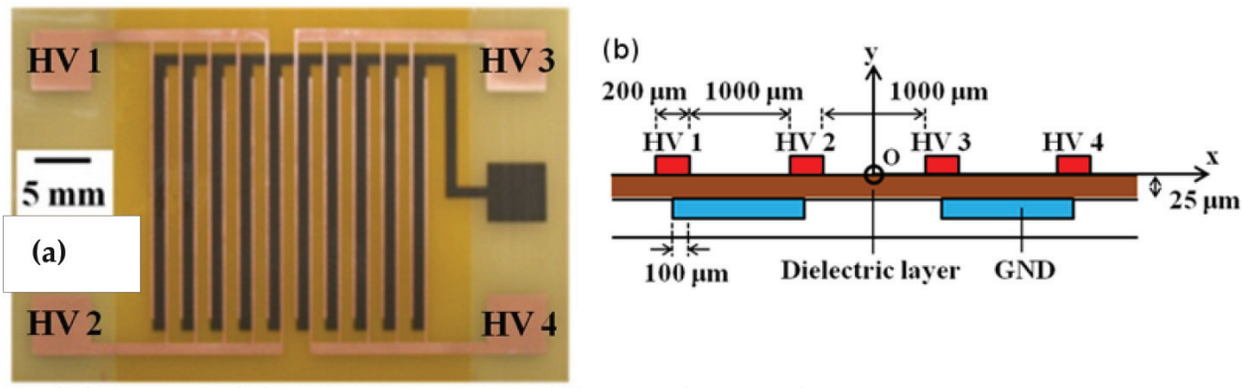

Figure 10. Microplasma actuator. Schematic image. Top-view showing (a) 20 strip-like electrodes and (b) cross-sectional view.

shown in **Figure 2** was developed. The schematic of a DBD microplasma actuator is shown in **Figure 10** [32, 41]. It consists of 20 strip-like electrodes with a 200 µm width and 16 µm thickness (top-side electrode) which are placed above a plate-like electrode (bottom-side electrode) with a dielectric layer of 25 µm thicknesses in between. Electrodes were made of copper and the dielectric layer was made of resin film. The gap is in micrometer order; thus, if only 1.4 kV is applied, the value of the obtained electric field is high (~10^7–10^8 V/m). This can be considered a low voltage and thus is easier to control and insulate and furthermore requires smaller sized power supplies. The resin film is a flexible polymer material that makes the microplasma actuator suitable for bending and attaching to various shapes, thus making the actuator suitable for flow control applications.

The flow was visualized using particle tracking velocimetry (PTV) [45]. Sub-micron size incense smoke was used as tracer particle and a Nd YVO4 532 nm laser was utilized to visualize the flow as shown in **Figure 4**. The phenomena induced by the microplasma actuator, was measured using a high-speed camera.

In the left part of the actuator ($x < 0$), the strips which were energized were marked as HV1 while the other strips were at floating potential as shown in **Figure 10**. The energized electrodes in the right part of the actuator ($x > 0$) were marked as HV4 while the other strips were at floating potential. The electrodes below the dielectric layer were grounded. The duty ratio of the actuator is defined as D by subtracting from 100% the duty ratio of the voltage applied to the HV4 electrodes. The duty ratios of HV1 and HV4 have a sum of 100%.

A duty ratio of $D = 80\%$ represents a duty ratio of 20% for the HV4 electrodes and a duty ratio of 80% for the HV1 electrodes.

The waveform of the applied voltage with $D = 20\%$ is shown in **Figure 11**. The peak of the AC applied voltage was 1.4 kV at a 20 kHz frequency. The burst frequency for the applied voltage was 4 kHz.

In the initial stages of the discharge, vortexes appeared near the active electrodes as shown in **Figure 12** at 2.5 and 5 ms, respectively. The duty ratio was $D = 20\%$; thus, the vortexes near the HV1 electrodes are rotating counter-clockwise and the vortexes near the HV4 electrodes are rotating clockwise. The flow velocity is higher for the HV1 electrodes since the duty ratio is 20% (HV1 electrodes are energized for a shorter time compared with HV4 electrodes). Gradually, the vortexes join together and leftward flow is established up to 50 ms.

2.2. Numerical simulation study of microplasma actuator

We have developed a numerical simulation code based on the Suzen model [33, 34]. According to the model, the EHD force is:

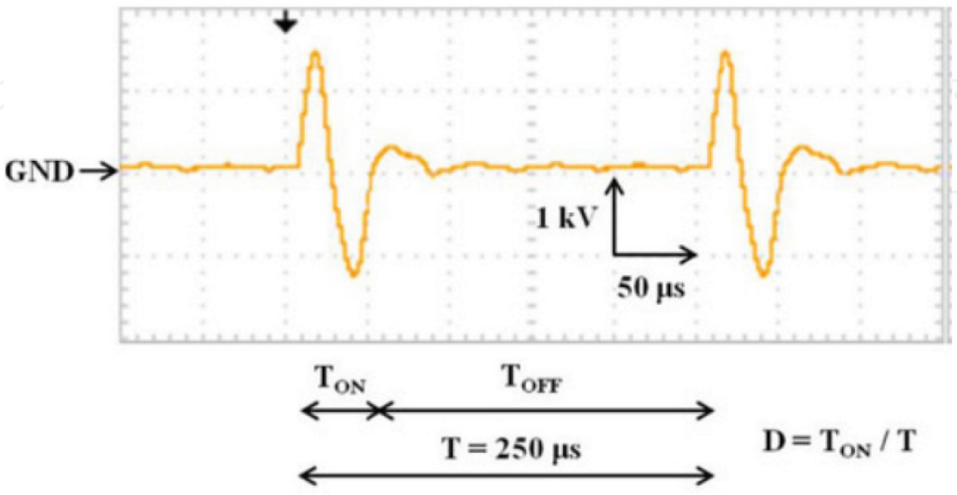

Figure 11. Waveform of applied voltage. The duty ratio is the ratio between the time in which the voltage is on and the sum of the time on plus time off.

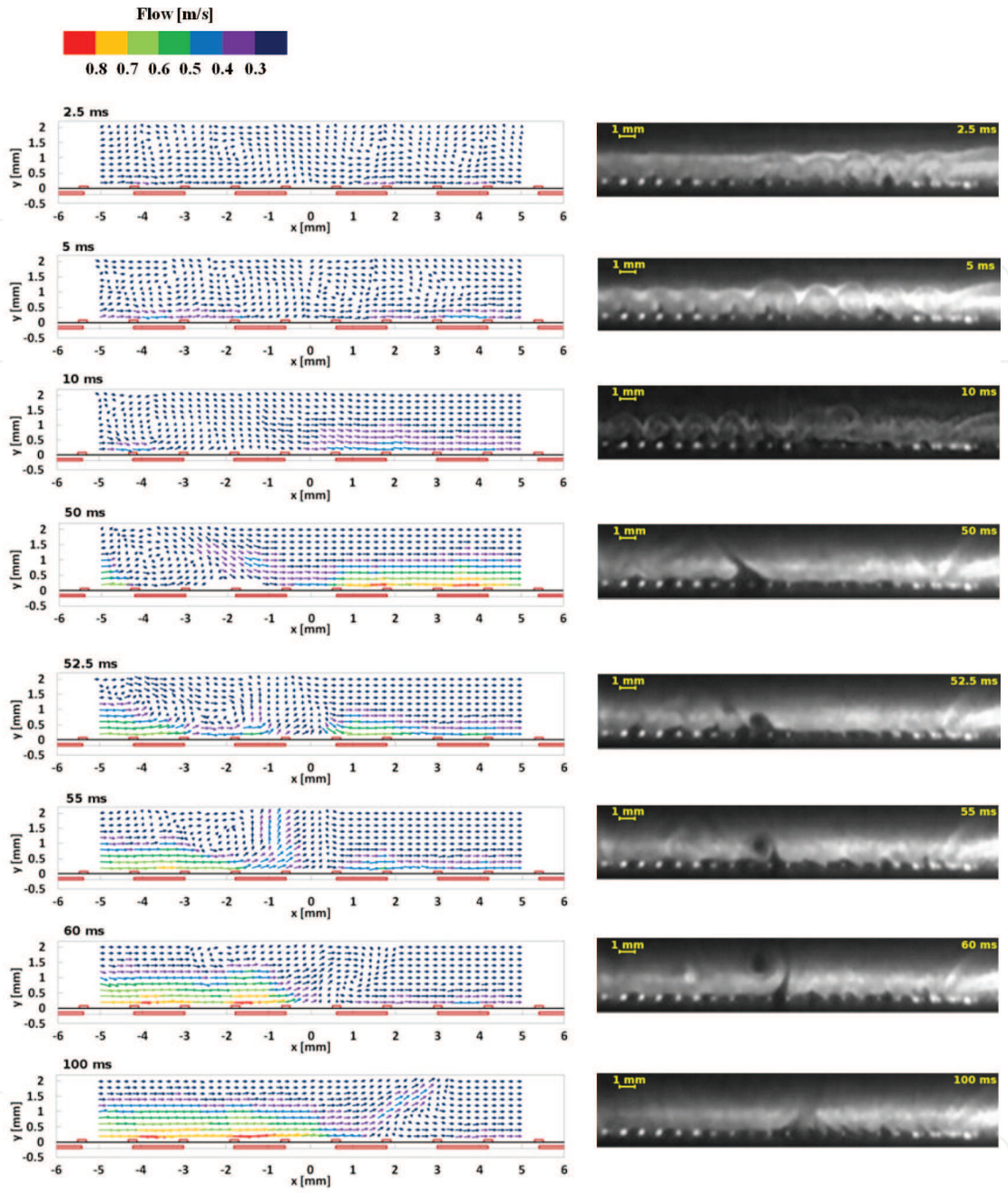

Figure 12. PTV results for four active electrodes (left side) and images of the flow for the entire actuator (right side). D = 20% up to 50 ms and D = 70% for more than 50 ms.

$$\vec{f} = \rho_c \cdot \vec{E}\,, \tag{1}$$

where f represents the body force per unit volume, ρ_c represents the net charge density, and E represents the intensity of the electric field. In this model, magnetic forces were considered. Furthermore, the electric field:

$$\vec{E} = -\nabla V \tag{2}$$

where V represents the potential. Gauss' law is written as:

$$\nabla\left(\varepsilon\cdot\vec{E}\right)=\rho_c \tag{3}$$

and furthermore:

$$\nabla(\varepsilon\cdot\nabla V)=-\rho_c \tag{4}$$

where ε represents the permittivity that was calculated as the product of relative permittivity ε_r and the permittivity of free space ε_0. Using the potential V and the Debye length $\lambda_{D,}$ the charge density is expressed as [33, 34]:

$$\frac{\rho_c}{\varepsilon_0}=\left(\frac{-1}{\lambda_D^2}\right)V. \tag{5}$$

Using Eqs. (1) and (5), the body force is calculated. In the Suzen model, it is assumed that the gas particles are weakly ionized; thus, the potential V can be decoupled in a potential due to the external electric field Ø and a potential due to the net charge density φ [33, 34]:

$$V=\phi+\varphi \tag{6}$$

Two independent equations can be written as:

$$\nabla\left(\varepsilon_r\cdot\nabla\phi\right)=0 \tag{7}$$

$$\nabla(\varepsilon_r\cdot\nabla\varphi)=\frac{-\rho_c}{\varepsilon_0}. \tag{8}$$

If we consider:

$$\frac{\rho_c}{\varepsilon_0}=\left(\frac{-1}{\lambda_D^2}\right)\varphi \tag{9}$$

We can write Eq. (8) as:

$$\nabla(\varepsilon_r\cdot\nabla\rho_c)=\frac{\rho_c}{\lambda_D^2} \tag{10}$$

Furthermore, the body force is calculated by

$$\vec{f}=\rho_c\cdot\vec{E}=\rho_c(-\nabla\varphi) \tag{11}$$

The permittivity between the dielectric and air was considered as the harmonic mean between dielectric permittivity taken as $\varepsilon_{rd}=4$ and air permittivity $\varepsilon_{rair}=1$; thus, the electric field was conserved [33]. Neumann boundary conditions were used for Eq. (7) as outer boundary conditions:

$$\frac{\partial \varphi}{\partial n} = 0 \tag{12}$$

Dirichlet boundary conditions were used for Eq. (10) as the outer boundary conditions:

$$\rho_c = 0. \tag{13}$$

In the numerical simulation code, in the dielectric, the values of u and v were 0. Using Eq. (10), the charge distribution over the encapsulated electrode was calculated considering the covered electrodes as the source charge. A value of $\rho c = 0.00751$ C/m^3 was used for the source charge. The same values as Suzen [34] were used for the Debye length with $\lambda_D = 0.00017$ m for air and $\lambda_D = \infty$ for the dielectric. Good agreement with experimental data was obtained for these values. After solving Eq. (11), the value of the body force was inserted in the Navier-Stokes equations:

$$\frac{\partial u}{\partial t} + u\frac{\partial u}{\partial x} + v\frac{\partial u}{\partial y} = \frac{-1}{\rho}\frac{\partial p}{\partial x} + \upsilon\left(\frac{\partial^2 u}{\partial x^2} + \frac{\partial^2 u}{\partial y^2}\right) + Fx \tag{14}$$

$$\frac{\partial v}{\partial t} + u\frac{\partial v}{\partial x} + v\frac{\partial v}{\partial y} = \frac{-1}{\rho}\frac{\partial p}{\partial y} + \upsilon\left(\frac{\partial^2 v}{\partial x^2} + \frac{\partial^2 v}{\partial y^2}\right) + Fy \tag{15}$$

$$\frac{\partial^2 p}{\partial x^2} + \frac{\partial^2 p}{\partial y^2} = -\rho\left(\frac{\partial u}{\partial x}\frac{\partial u}{\partial x} + 2\frac{\partial u}{\partial y}\frac{\partial v}{\partial x} + \frac{\partial v}{\partial y}\frac{\partial v}{\partial y}\right) \tag{16}$$

where u and v represent the components of the flow velocity on the x-axis and y-axis, ρ is the fluid density, p is the pressure, and υ is the kinematic viscosity. The dynamic viscosity μ is written as:

$$\mu = \varrho\, \upsilon \tag{17}$$

We have used for the air density, ρ = 1.177 kg/m^3 and for the kinematic viscosity, $\upsilon = 1.57 \times 10^{-5}$ m^2/s; thus, the calculated dynamic viscosity $\mu = 1.8 \times 10^{-5}$ kg/ms. The computational geometry is shown in **Figure 13**. The dimensions of the grid were 14 × 14 mm with 561 × 561 grid points. For solving Eqs. (7) and (10), the convergence parameter was 10^{-8}. A projection method in primitive variables on a collocated mesh was used for solving the Navier-Stokes equations.

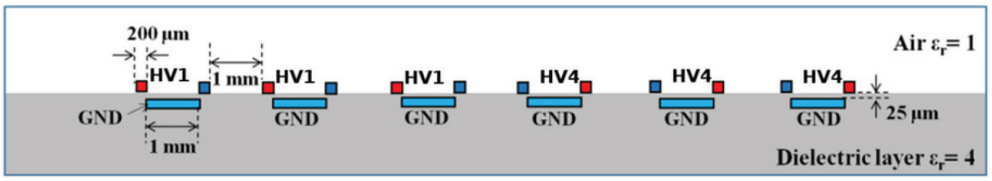

Figure 13. Computational geometry. Upper electrodes HV1 and HV4 were energized and the encapsulated electrodes were grounded.

The microplasma actuator shown in the experimental part had 20 strip-like exposed electrodes. These conditions while keeping a high mesh density necessary for accurate results will also increase the simulation time; thus, we chose for the numerical simulation, 12 exposed electrodes and 6 covered electrodes as shown in **Figure 13**. The energized electrodes were labeled HV1 (3 electrodes) and HV4 (3 electrodes). In the experimental part, the electrodes were energized at an AC waveform having an amplitude of 1.4 kV and a frequency of 20 kHz. The signal was modulated at 4 kHz with duty ratios of 20, 30, 70, and 80%. Considering that the effective value of 1.4 kV peak is 1 kV, we chose for computational reasons for the simulation that the applied voltage is a positive pulse signal with a peak value of 1 kV. Duty ratios for the positive pulse were 20, 30, 70, and 80% as shown in **Figure 14**.

Eqs. (7), (10), and (11) were solved to obtain the potential of the external electric field Ø, the potential of the net charge density φ, and the body force. These were calculated before solving the Navier-Stokes, as shown in **Figure 15**. Near the active electrodes HV1 and HV4, high values of the body force were calculated. For developing the numerical simulation code, the Julia programming language was used [54]. The same duty ratios were used as in the experimental part: first case when electrodes HV1 were energized at 20% duty ratio and HV4 electrodes were energized at 80%; thus, the actuator duty ratio D = 20%, and second case where HV1 electrodes were energized at 70% duty ratio and HV4 electrodes were energized

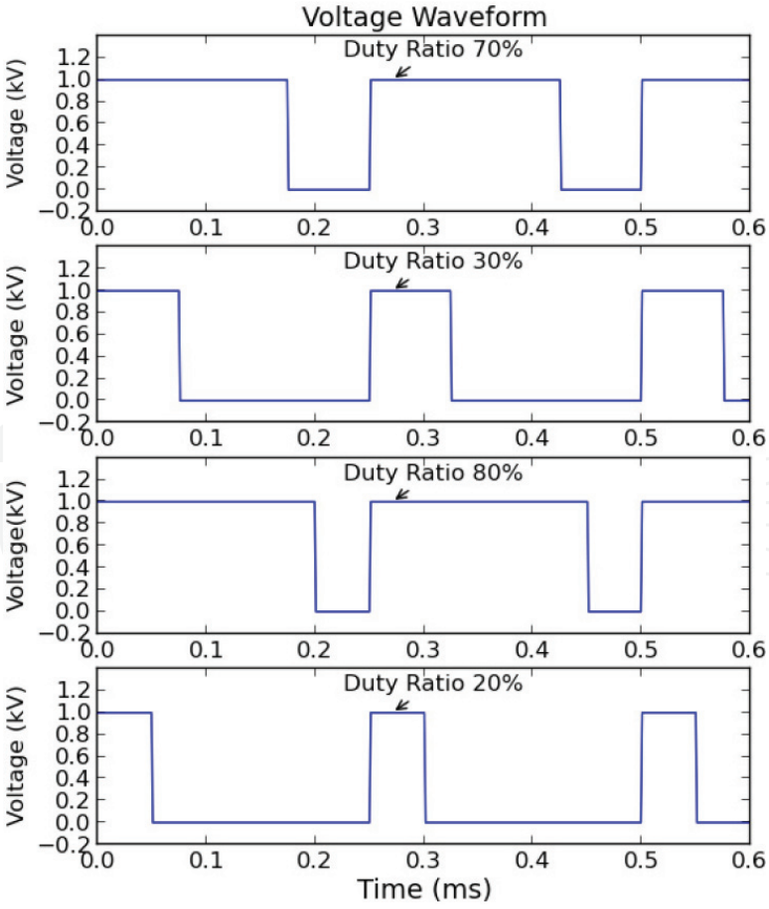

Figure 14. Simulation voltage waveforms. Positive pulse with duty ratio of 70, 30, 80, and 20%.

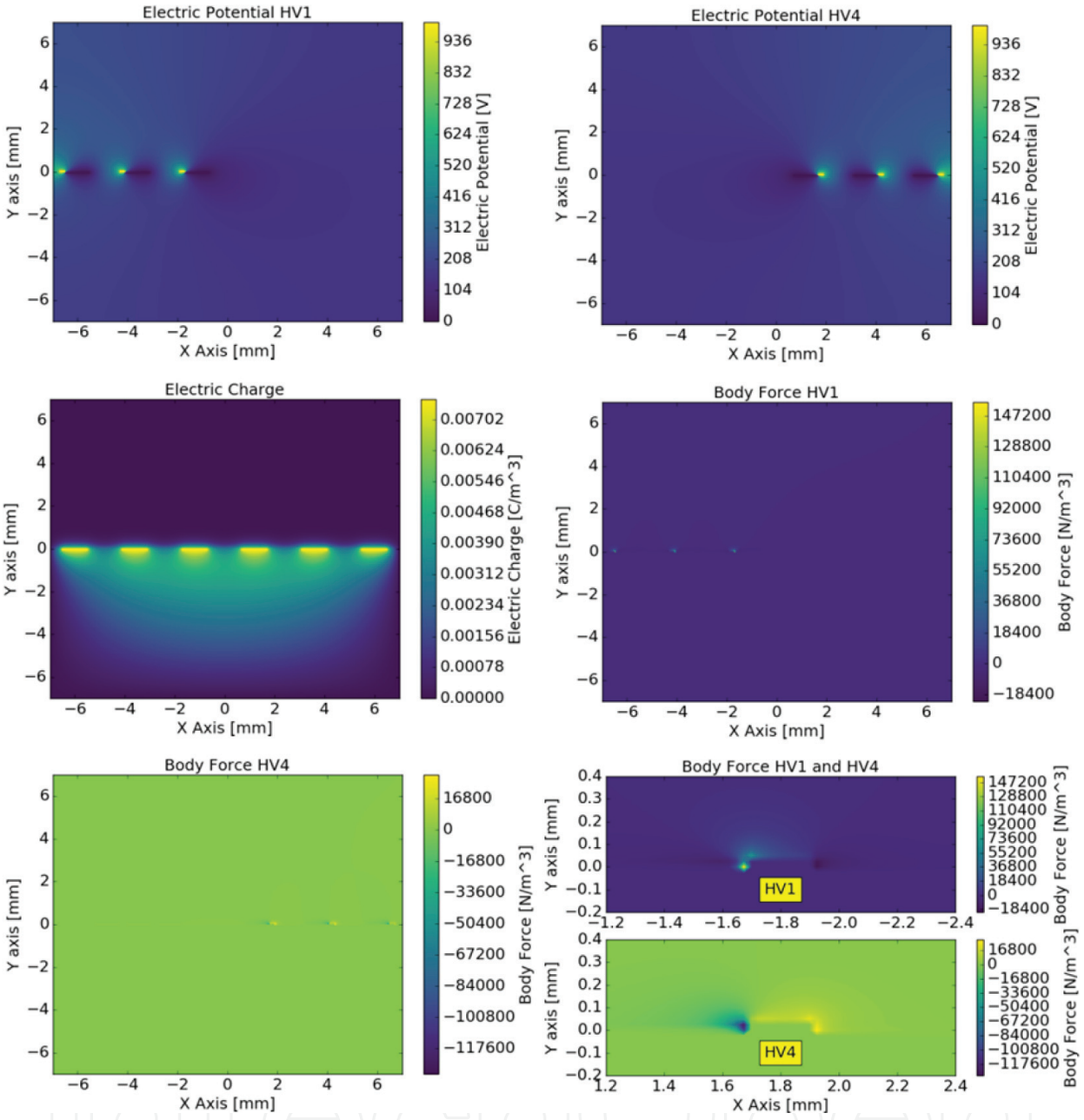

Figure 15. Calculated electric potential, charge density, and body force: Electrodes HV1 and HV4 = 1000 V; covered electrode = 0 V. Higher values of body force were obtained near the active exposed electrodes (shown in HV1 and HV4 enlarged).

at 30%; thus, actuator duty ratio D = 70%. The results for D = 20% are shown in **Figure 16**. Vortexes appeared in the initial stages of the phenomena up to 5 ms. As was observed also in the experimental results, the vortexes appeared above the covered electrodes and had a counter-clockwise direction near the HV1 electrodes and clockwise direction near the HV4 electrodes. With the lapse of time at t = 10 ms, the vortexes moved up; thus, at 15 ms, it can be observed that the vortexes start to join together and create a flow directed diagonal to the left. At 50 ms, the flow is in a steady state with an extended diagonal flow toward the left as

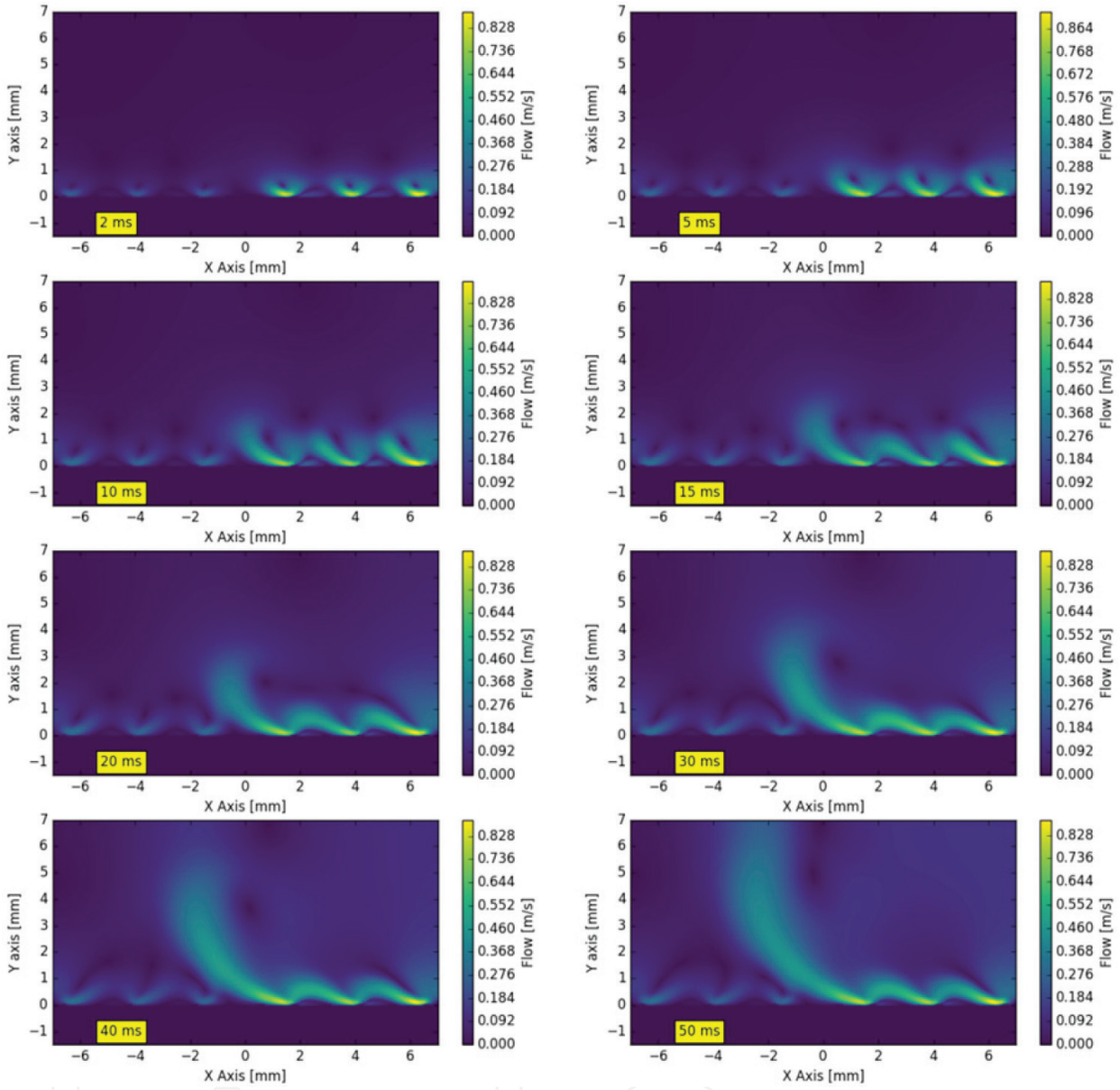

Figure 16. Flow: Flow for duty ratio D = 20%: Initial vortexes appeared (2 ms); vortexes increase in size (10 ms); leftward flow steady state (50 ms).

observed in the experimental results. The maximum calculated value of the flow of 0.83 m/s was near the active electrodes and the value of the flow in the diagonal direction was 0.45 m/s. The PTV measured value of the diagonal flow was 0.43 m/s, which is in agreement with numerical simulations. The duty ratio of the actuator after 50 ms was D = 70%.

In **Figure 17** are shown the simulation results for D = 70%. The electrodes HV1 are energized for a longer time compared with HV4 electrodes; thus, the flow near the HV1 electrodes is faster. The direction of the diagonal flow obtained up to 50 ms is changing gradually, from leftward to rightward as measured by the PTV method. Vortexes are observed near the HV1 electrodes up to 55 ms. A complete tilt toward the right part is observed at 80 ms. At 120 ms, it can be considered that a steady state was achieved.

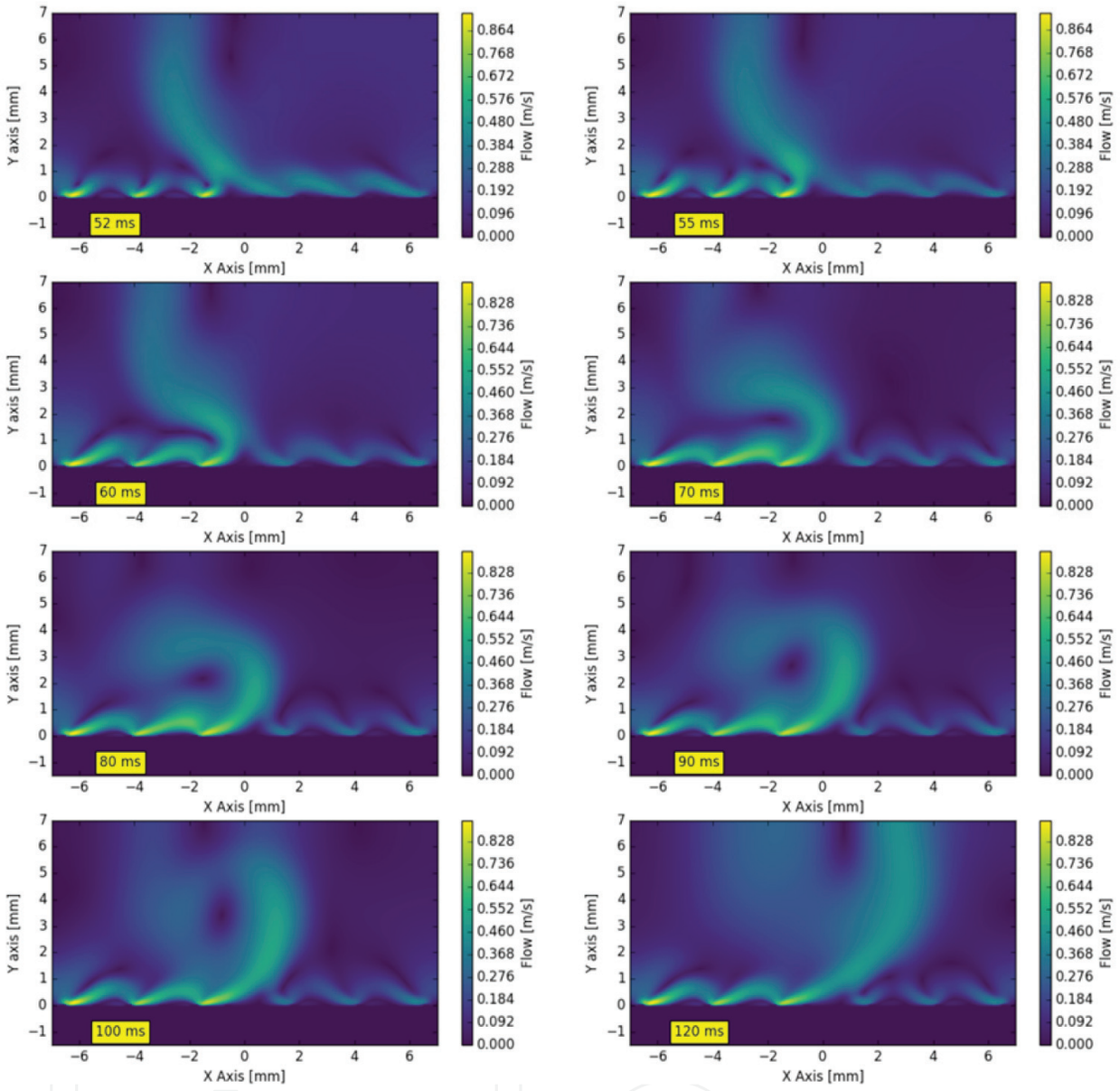

Figure 17. Flow for duty ratio D = 70%: After 50 ms, the leftward diagonal flow is changing gradually to rightward diagonal flow.

The maximum values of the flow of 0.82 m/s were calculated near the HV1 electrodes. For the diagonal flow, the value was 0.43 m/s. The value obtained by PTV method was 0.42 m/s for the diagonal flow. In the case of experimental results, due to the microplasma light emission near the active electrodes, the flow could not be measured properly; thus, the simulation gave us valuable insight into the microplasma actuator phenomena. The leftward diagonal flow obtained at D = 20% has a smaller angle with the horizontal axis compared with the rightward diagonal flow at D = 70%.

3. Conclusions

A microplasma actuator is a device with no moving parts that has advantages over conventional actuators. It can be energized at voltages of about 1 kV, and thus requires a smaller size power supply and less electrical insulation compared with macro-plasma actuators. Moreover, due to the use of pulse voltage to energize the actuator, the energy consumption is low.

The use of a microplasma actuator for flow control showed the capability of the actuator to induce flow and also to change the direction of the flow. By using devices with field-effect transistor (FET) switches to energize the actuator, the flow direction was changed from diagonal leftward to diagonal rightward when the duty ratio of applied voltage was changed. This could be useful if the actuator were to be attached to small drones. The characteristics of the flow were investigated both experimentally and using numerical simulations. A numerical simulation code was developed based on the Suzen-Huang model, which calculates the body force from the potential of the external electric field and the potential of the charge density of the plasma, and implements the body force in Navier-Stokes equations. The experimental results confirmed the validity of the developed code.

Acknowledgements

The authors would like to thank Professor Hitoki Yoneda from the University of Electro-Communications, Tokyo, Professor Damon Chandler, Mr. Yoshinori Mizuno, Mr. Akihiko Ito and Mr. Daisuke Nonaka from Shizuoka University, Hamamatsu, for the fruitful discussions.

Author details

Kazuo Shimizu* and Marius Blajan

*Address all correspondence to: shimizu@cjr.shizuoka.ac.jp

Shizuoka University, Hamamatsu, Japan

References

[1] Gadelhak M. Flow Control. Cambridge: Cambridge University Press; 2000

[2] Roth JR, Din X. Optimization of the aerodynamic plasma actuator as an electrohydrodynamic (EHD) electrical device. In: Proceedings of the 44th AIAA Aerospace Sciences Meeting Exhibit; January 9–12, 2006. DOI: 10.2514/6.2006-1203

[3] Singh KP, Roy S. Impedance matching for an asymmetric dielectric barrier discharge plasma actuator. Journal of Applied Physics. 2008;**103**:013305

[4] Neumann M, Friedrich C, Kriegseis J, Grundmann S, Czarske J. Determination of the phase-resolved volume force produced by a dielectric barrier discharge plasma actuator. Journal of Physics D: Applied Physics. 2013;**46**:042001

[5] Jacob JD, Ramakumar K, Anthony R, Rivir RB. Control of laminar and turbulent shear flows using plasma actuators. In: Proceedings of the 4th International Symposium Turbulence Shear Flow Phenomena; June 27–29, 2005

[6] Im S, Do H, Cappelli MA. Dielectric barrier discharge control of a turbulent boundary layer in a supersonic flow. Applied Physics Letters. 2010;**97**:041503

[7] Goksel B et al. Pulsed plasma actuators for separation flow control. In: Proceedings of the Conference Turbulence Interactions; 2006. DOI: 10.13140/RG.2.1.2275.5925

[8] Thomas FO, Kozlov A, Corke TC. Plasma actuators for bluff body flow control. Journal of AIAA. 2008;**46**(8):1921-1931

[9] Li Y, Zhang X, Huang X. The use of plasma actuators for bluff body broadband noise control. Experiments Fluids. 2010;**49**:367-377

[10] Benard N, Moreau E. Electrical and mechanical characteristics of surface AC dielectric barrier discharge plasma actuators applied to airflow control. Experiments in Fluids. 2014; **55**:1846. DOI: 10.1007/s00348-014-1846-x

[11] Zhao L, Adamiak K. Electrohydrodynamic flow produced by electric corona discharge (numerical and experimental studies, and applications). In: Proceedings of the 2009 Electrostatics Joint Conference, Boston, P2.13; June 16–18, 2009

[12] Colas DF, Ferret A, Pai DZ, Lacoste DA, Laux CO. Ionic wind generation by a wire-cylinder-plate corona discharge in air at atmospheric pressure. Journal of Applied Physics. 2010;**108**:103306

[13] Robinson M. Movement of air in the electric wind of the corona discharge. Transactions of the American Institute of Electrical Engineers. 1961;**80**:143-150

[14] June MS, Kribs J, Lyons KM. Measuring efficiency of positive and negative ionic wind devices for comparison to fans and blowers. Journal of Electrostatics. 2011;**69**:345-350

[15] Kim C, Park D, Noh KC, Hwang J. Velocity and energy conversion efficiency characteristics of ionic wind generator in a multistage configuration. Journal of Electrostatics. 2010; **68**:36-41

[16] Touchard G. Plasma actuators for aeronautics applications – state of art review. IJPEST. 2008;**2**(1):1-25

[17] Whalley RD, Choi K-S. The starting vortex in quiescent air induced by dielectric-barrier-discharge plasma. Journal of Fluid Mechanics. 2013;**703**:192203

[18] Whalley RD, Choi K-S. Turbulent boundary-layer control with plasma spanwise travelling waves. Experiments in Fluids. 2014;**55**:1796

[19] Choi K-S, Jukes T, Whaley R. Turbulent boundary-layer control with plasma actuators. Philosophical Transactions of the Royal Society A. 2011;**369**:1443-1458

[20] Wang C-C, Roy S. Microscale plasma actuators for improved thrust density. Journal of Applied Physics. 2009;**106**:013310

[21] Wang C-C, Roy S. Energy and force prediction for a nanosecond pulsed dielectric barrier discharge actuator. Journal of Applied Physics. 2012;**111**:103302

[22] Shyy W, Jayaraman B, Andersson A. Modeling of glow discharge-induced fluid dynamics. Journal of Applied Physics. 2002;**92**(11):6434-6443

[23] Shimizu K, Mizuno Y, Blajan M. Basic study on force induction using dielectric barrier microplasma array. Japanese Journal of Applied Physics. 2015;**54**:01AA07

[24] Santhanakrishnan A, Jacob J. On plasma synthetic jet actuators. In: 44th AIAA Aerospace Science Meeting and Exhibit, Reno; January 9–12, 2006. p. 685

[25] Bolitho M, Jacob J. Active vortex generators using jet vectoring plasma actuators. SAE International Journal of Aerospace. 2008;**1**(1):610-618

[26] Bénard N, Jolibois J, Moreau E, Sosa R, Artana G, Touchard G. Aerodynamic plasma actuators: A directional micro-jet device. Thin Solid Films. 2008;**516**:6660-6667

[27] Neretti G, Cristofolini A, Borghi CA. Experimental investigation on a vectorized aerodynamic dielectric barrier discharge plasma actuator array. Journal of Applied Physics. 2014; **115**:163304

[28] Shimizu K, Kuwabara T, Blajan M. Study on decomposition of indoor air contaminants by pulsed atmospheric microplasma. Sensors. 2012;**12**(11):14525-14536

[29] Blajan M, Shimizu K. Temporal evolution of dielectric barrier discharge microplasma. Applied Physics Letters. 2012;**101**:104101

[30] Shimizu K, Blajan M, Tatematsu S. Basic study of remote disinfection and sterilization effect by using atmospheric microplasma. IEEE Transactions on Industry Applications. 2012;**48**:1182-1188

[31] Blajan M, Umeda A, Muramatsu S, Shimizu K. Emission spectroscopy of pulsed powered microplasma for surface treatment of PEN film. IEEE Transactions on Industry Applications. 2011;**47**:1100-1108

[32] Mizuno Y, Blajan M, Yoneda H, Shimizu K. Active fluid control by multi-electrode microplasma actuator. Journal of Institute of Electrostatics Japan. 2015;**39**:15 [in Japanese]

[33] Suzen YB, Huang PG, Jacob JD, Ashpis DE. Numerical simulations of plasma based flow control applications. In: 35th Fluid Dynamics Conference and Exhibit; June 6–9, 2005; Toronto. AIAA. pp. 2005-4633

[34] Suzen YB, Huang PG, Ashpis DE. Numerical simulations of flow separation control in low-pressure turbines using plasma actuators. In: 45th AIAA Aerospace Sciences Meeting and Exhibit; January 8–11, 2007; Reno. AIAA; 2007. p. 937

[35] Orlov DM. Modelling and simulation of single dielectric barrier discharge plasma actuator. PhD thesis, University of Notre Dame; 2006

[36] Unfer T, Boeuf JP. Modeling of a nanosecond surface discharge actuator. Journal of Physics D: Applied Physics. 2009;**42**:194017

[37] Likhanskii AV, Shneider MN, Macheret SO, Miles RB. Modeling of dielectric barrier discharge plasma actuator in air. Journal of Applied Physics. 2008;**103**:053305

[38] Nishida H, Abe T. Numerical analysis for plasma dynamics in SDBD plasma actuator. In: 41st Plasma Dynamics and Lasers Conference; June 28–July 1, 2010

[39] Bai J, Sun J, Zhang Q, Wang D. PIC simulation of RF hydrogen discharges in a transverse magnetic field. Current Applied Physics. 2011;**11**:S140-S144

[40] Mahfoze O, Laizet S. Skin-friction drag reduction in a channel flow with streamwise-aligned plasma actuators. International Journal of Heat and Fluid Flow. 2017;**66**:83-94

[41] Blajan M, Mizuno Y, Ito A, Shimizu K. Microplasma actuator for EHD induced flow. IEEE Transaction on Industry Applications. 2017;**53**(3):2409-2415

[42] Moreau E, Sosa R, Artana G. Electric wind produced by surface plasma actuators: A new dielectric barrier discharge based on a threeelectrode geometry. Journal of Applied Physics. 2008;**41**:115204

[43] Dawson R, Little J. Characterization of nanosecond pulse driven dielectric barrier discharge plasma actuators for aerodynamic flow control. Journal of Applied Physics. 2013; **113**:103302

[44] Shimizu K, Mizuno Y, Blajan M, Yoneda H. Characteristics of an atmospheric nonthermal microplasma actuator. IEEE Transaction on Industry Applications. 2017;**53**(2):1452-1458

[45] Fu S, Biwole PH, Mathis C. Particle tracking velocimetry for indoor airflow field: A review. Building and Environment. 2015;**87**:34-44

[46] Pescini E, Giorgi MGD, Francioso L, Sciolti A, Ficarella A. Effect of amicro dielectric barrier discharge plasma actuator on quiescent flow. Science, Measurement and Technology. 2014;**8**(3):135-142

[47] Yoon SY, Ross JW, Mench MM, Sharp KV. Gas-phase particle image velocimetry (PIV) for application to the design of fuel cell reactant flow channels. Journal of Power Sources. 2006;**160**:1017-1025

[48] Celestin S, Bonaventura Z, Guaitella O, Rousseau A, Bourdon A. Influence of surface charges on the structure of a dielectric barrier discharge in air at atmospheric pressure: Experiment and modeling. European Physical Journal Applied Physics. 2009;**47**(2):22810

[49] Bronold FX, Fehske H, Heinisch RL, Marbach J. Wall charge and potential from a microscopic point of view. Contributions to Plasma Physics. 2012;**52**:356-863

[50] Pietscha GJ, Gibalovb VI. Dielectric barrier discharges and ozone synthesis. Pure and Applied Chemistry. 1998;**70**(6):1169-1174

[51] Buntat Z, Smith IR, Razali NAM. Ozone generation by pulsed streamer discharge in air. Applied Physics Research. 2009;**2**:1

[52] Tanaka M, Ogawa S, Wada N, Yoshiyasu H, Yagi S. Influence of rust on electrodes of oxygen-fed ozonizer to ozone generation. IEEJ Transactions on Fundamentals and Materials. 2006;**125**(10):817-822

[53] Kawamoto H, Koboyashi T. Ozone generation in plasma actuator. Japan Society of Mechanical Engineers Series B. 2009;**75**(759):2345-2347

[54] 2018. [Online]. Available: http://julialang.org

IntechOpen